First-principles calculations for the tunnel ionization rate of atoms and molecules

T. Otobe and K. Yabana
Institute of Physics, University of Tsukuba, Tsukuba 305-8571, Japan

J.-I. Iwata
Nanotechnology Research Institute, Advanced Industrial Science and Technology, Tsukuba 305-8568, Japan
(Received 7 November 2003; published 7 May 2004)

We present first-principles calculations for the tunnel ionization rate of some atoms and molecules in a static intense electric field. The Gamow state is calculated to describe the ionization process in the Kohn-Sham formalism with the self-interaction correction. The tunnel ionization rate is obtained from the imaginary part of the Gamow state eigenvalue. The ionization rates of rare-gas atoms Ar and Xe and diatomic molecules N_2, O_2, and F_2 are investigated. The calculations describe well the observed behavior of the tunnel ionization. The results also show good correspondence with the Ammosov-Delone-Krainov model for rare-gas atoms. We find that the properties of the highest occupied orbital have significant effects on the ionization rate. In particular, our calculation reproduces the suppression of the ionization rate of O_2 molecule in comparison with that of Xe atom. We also find that the ionization rates of O_2 and F_2 molecules are very sensitive to the relative angle between the electric field and the molecular axis, reflecting properties of the highest occupied orbital.

DOI: 10.1103/PhysRevA.69.053404 PACS number(s): 33.80.Rv, 42.50.Hz

I. INTRODUCTION

Atoms and molecules under intense laser field show interesting electron dynamics when the strength of the external electric field is comparable to the strength of the self-consistent field inside them. Among various phenomena under intense laser field, the change of the ionization mechanism depending on the laser intensity has attracted considerable interests. The key parameter which controls the ionization mechanism is the Keldysh parameter $\gamma = \omega\sqrt{2I_P}/F$ [1], where ω is the frequency of the external field, I_P is the ionization potential, and F is the strength of the field. The multiphoton ionization is expected to dominate when $\gamma > 1$, while the direct electron emission through either tunnel or above barrier processes dominates when $\gamma < 1$.

To describe the ionization rates, analytical expressions have been derived. The Ammosov-Delone-Krainov (ADK) model [2] is based on the quasistatic approximation and has been applied for ionization of atoms with success. The Keldysh-Faisal-Reiss model [1,3,4] is an alternative approach which takes into account the time dependence of the external field.

Besides these analytical approaches, various computational approaches have been rapidly developed to describe the electron dynamics under the intense laser field. For example, the high harmonic generation in atoms has been analyzed by solving the time-dependent Schrödinger equation in the single-electron approximation [5]. A coupled dynamics of an electron and ions for H_2^+ is a three-body problem and has been studied in Refs. [6–9]. For atoms and molecules with many electrons, the time-dependent density-functional theory (TD-DFT) has been extensively applied [10–14]. The TD-DFT calculations offer an *ab initio* description of the many-electron dynamics, and have been providing insights into various nonlinear electron dynamics. They are, however, achieved mostly for problems with an axial symmetry. There are a number of subjects which await three-dimensional descriptions: for example, the ionization of molecule when the external field is not parallel to the molecular axis, the ionization of atoms by a laser with circular polarization, and so on.

We have been developing a three-dimensional computation of the many-electron dynamics in the TD-DFT in which the time-dependent Kohn-Sham equation is solved in real time and real space. The method has been most successful to describe linear optical responses [15–18]. It has recently been extended to the perturbative nonlinear responses [19]. The multielectron transfer dynamics under strong field induced by the highly charged ion was also studied in Ref. [20].

In this paper, we present a first-principles, three-dimensional calculations for the tunnel ionization rates of atoms and molecules. We present results of the ionization rates of neutral atoms and molecules under a static external field. We expect these static results will provide useful information to understand the basic mechanism of the tunnel ionization. The static treatment may be justified for rare-gas atoms and small molecules, since the frequency of the laser field is usually much smaller than the frequencies of the lowest electronic excitations.

It has been known that the tunnel ionization rates of atoms and molecules depend crucially on their ionization potentials. The tunnel ionization rates of atoms and molecules with approximately the same ionization potential are usually close to each other. Recently, however, the ionization rate of O_2 molecule is found to be much smaller than that of Xe atom, although their ionization potentials are almost the same [21,22,29]. Regarding the origin of this difference, several explanations have been put forward [22,23]. Recently, an extension of the ADK theory incorporating the properties of molecular orbitals has been presented [24] where the importance of the orbital properties of molecules was stressed. We will clarify, by our microscopic calculations, that the properties of the molecular orbitals are indeed responsible for the suppression of the ionization rate of O_2 molecule.

To describe the ionization rates of diatomic molecules with the external field being not parallel to the molecular axis, we must treat a decaying state without any spatial symmetries. We have developed a computational approach in which the Gamow state is constructed based on the Kohn-Sham formalism in the DFT. The decaying boundary condition is approximately described by introducing an absorbing boundary condition. The ionization rate is then obtained from the imaginary part of the eigenvalue. In the calculation, the orbital wave functions are represented on the grid points in the three-dimensional curvilinear coordinates.

The organization of the present paper is as follows. In Sec. II, we present our formalism to calculate ionization rate in the Kohn-Sham framework. In Sec. III, we show our results for the rare-gas atoms Ar and Xe and some diatom molecules N_2, O_2, and F_2. In Sec. IV, summary will be presented.

II. FORMULATION

A. Gamow state in the Kohn-Sham formalism

We will employ the Kohn-Sham formalism in the DFT to calculate the tunnel ionization rate. Since the DFT is a theory for the electronic ground state, we first clarify the grounds that the DFT can be applicable to calculate the ionization rate. We rely upon the TD-DFT for this purpose.

We consider a molecule under an intense, time-dependent electric dipole field. We express the interaction potential between the electrons in the molecule and the external field as $V_{\rm ext}(\vec{r},t)=eF(t)z$ where $F(t)$ is the strength of the time-varying dipole field. This external perturbation induces electron emission to the continuum. Since the ionization rate is proportional to the number of electrons which pass through a sphere of large radius per unit time (averaged over a certain time period), the ionization rate is calculated from the time-dependent electron density $n(\vec{r},t)$. In the TD-DFT, the time evolution of the electron density is described by the time-dependent Kohn-Sham equation,

$$i\hbar\frac{\partial}{\partial t}\psi_i(t)=\{h[n(\vec{r},t)]+V_{\rm ext}(t)\}\psi_i(\vec{r},t), \tag{1}$$

$$n(\vec{r},t)=\sum_i|\psi_i(\vec{r},t)|^2. \tag{2}$$

The Kohn-Sham Hamiltonian $h[n(\vec{r},t)]$ is given by

$$h[n(\vec{r},t)]=-\frac{\hbar^2}{2m}\nabla^2+V_{\rm ion}+e^2\int d\vec{r}'\frac{n(\vec{r}',t)}{|\vec{r}-\vec{r}'|}+\mu_{\rm xc}[n(\vec{r},t)], \tag{3}$$

where $V_{\rm ion}$ is the electron-ion potential and $\mu_{\rm xc}[n(\vec{r},t)]$ is the so-called exchange-correlation potential.

We now consider a case in which the external field changes very slowly in time. More precisely, we assume that the tunneling time is much shorter than the period of the external field. Namely, the Keldysh parameter γ is assumed to be much smaller than unity. We also assume the dominance of direct emission of electrons through either tunnel or above barrier processes, and ignore the multiphoton process. Under these circumstances, the time-dependent Kohn-Sham equation (1) is expected to yield the static Kohn-Sham equation with an external dipole field $V_{\rm ext}(\vec{r})=eFz$, where F is the strength of the electric field at a certain time.

$$\{h[n(r)]+V_{\rm ext}(\vec{r})\}\phi_i(\vec{r})=\epsilon_i\phi_i(\vec{r}). \tag{4}$$

Here the electrons in the molecule are continuously emitted to outside of the molecule so that the static Kohn-Sham orbitals $\phi_i(\vec{r})$ must satisfy the outgoing boundary condition without any incident waves. This is the so-called Gamow state. Because of the outgoing boundary condition, the orbital eigenvalues ϵ_i are complex numbers,

$$\epsilon_i=\epsilon_i^{\rm R}+i\Gamma_i. \tag{5}$$

where $\epsilon_i^{\rm R}$ and Γ_i are the real and the imaginary parts of ϵ_i.

The imaginary part of the eigenvalue Γ_i is related to the ionization rate. To see it, we multiply ϕ_i^* to Eq. (4) and subtract its complex conjugate:

$$-\frac{\hbar^2}{2m}(\phi_i^*\nabla^2\phi_i-\phi_i\nabla^2\phi_i^*)=2i\Gamma_i|\phi_i|^2. \tag{6}$$

We define the current density of the ith orbital $\vec{j}_i$ as usual,

$$\vec{j}_i=-\frac{i\hbar}{2m}(\phi_i^*\vec{\nabla}\phi_i-\phi_i\vec{\nabla}\phi_i^*). \tag{7}$$

Then we find

$$\vec{\nabla}\cdot\vec{j}_i=-\frac{2}{\hbar}\Gamma_i|\phi_i|^2. \tag{8}$$

Integrating both sides over the volume V which includes the molecule inside and employing the Gauss theorem, we have

$$\int_S\vec{n}\cdot\vec{j}_i dS=-\frac{2}{\hbar}\Gamma_i\int_V|\phi_i|^2d\vec{r}, \tag{9}$$

where S is the surface of the volume V, and $\vec{n}$ is a normal vector in the surface S. The ionization rate of the orbital i, w_i is now defined and is related to Γ_i as

$$w_i=\frac{\int_S\vec{n}\cdot\vec{j}_i dS}{\int_V|\phi_i|^2d\vec{r}}=-\frac{2}{\hbar}\Gamma_i. \tag{10}$$

The electrons emitted to the continuum, in principle, contribute to the self-consistent potential. If the ionization rate is very small, this contribution of emitted electrons to the potential will be small and negligible. Under this assumption, we will make calculations separating the procedure to calculate ionization rate into the following two steps: First, one solves the static Kohn-Sham equation under the static external field eFz. In this step, the tunnel ionization is forced to be prohibited by, for example, placing infinite wall potential outside the barrier. At this stage, the problem is a usual static Kohn-Sham problem except the appearance of the external dipole and infinite wall potentials. The second step is to cal-

culate the Gamow state solution for each Kohn-Sham orbital. At this stage, the Kohn-Sham Hamiltonian is kept fixed to that obtained in the previous step.

B. Kohn-Sham Hamiltonian

Because the ionization rate is sensitive to the asymptotic behavior of the potential as well as the orbital energies of the occupied orbitals, we should employ the exchange-correlation potential which is appropriate in these respects. We will employ the exchange-correlation potential which takes account of the self-interaction correction for this reason.

We adopt an approximate construction of the optimized effective potential including the self-interaction correction, which was proposed by Krieger, Li, and Iafrate (KLI) [25]. In this treatment, it has been shown that the ionization potentials of atoms and molecules approximately coincide with the energies of the highest occupied orbitals. The potential in this model also has a correct asymptotic behavior $-e^2/r$ for neutral molecules.

In the KLI prescription, the local, state-independent exchange-correlation potential $\mu_{\mathrm{xc},\sigma}^{\mathrm{SIC}}(\vec{r})$ is constructed by the following procedure:

$$\mu_{\mathrm{xc},\sigma}^{\mathrm{SIC}}(\vec{r}) = \sum_i \frac{\rho_{i\sigma}(\vec{r})}{\rho_\sigma(\vec{r})}\{v_{i\sigma}(\vec{r}) + [\overline{\mu}_{\mathrm{xc},i\sigma}^{\mathrm{SIC}} - \overline{v}_{i\sigma}]\}, \tag{11}$$

where $\rho_{i\sigma}(\vec{r})$ is the density of the ith orbital with spin σ. Other quantities are defined by

$$v_{i\sigma}(\vec{r}) = \frac{\delta E_{\mathrm{xc}}[\rho_\uparrow,\rho_\downarrow]}{\delta\rho_\sigma} - \int d\vec{r}'\frac{\rho_{i\sigma}(\vec{r}')}{|\vec{r}-\vec{r}'|} - \frac{\delta E_{\mathrm{xc}}[\rho_{i\sigma},0]}{\delta\rho_{i\sigma}}, \tag{12}$$

$$\overline{\mu}_{\mathrm{xc},i\sigma}^{\mathrm{SIC}} = \langle\psi_{i\sigma}|\mu_{\mathrm{xc},\sigma}^{\mathrm{SIC}}(\vec{r})|\psi_{i\sigma}\rangle, \tag{13}$$

$$\overline{v}_{i\sigma} = \langle\psi_{i\sigma}|v_{\mathrm{xc},\sigma}(\vec{r})|\psi_{i\sigma}\rangle. \tag{14}$$

$E_{\mathrm{xc}}[\rho_\uparrow,\rho_\downarrow]$ is the exchange-correlation energy density for spin-polarized electron gas. In the practical calculations, $[\overline{\mu}_{\mathrm{xc},i\sigma}^{\mathrm{SIC}} - \overline{v}_{i\sigma}]$ of Eq. (11) is calculated by solving the following algebraic equation:

$$\sum_{i=1}^{N_\sigma-1}(\delta_{ji,\sigma} - M_{ji,\sigma})(\overline{\mu}_{\mathrm{xc},i\sigma}^{\mathrm{SIC}} - \overline{v}_{i\sigma}) = \overline{V}_{j\sigma} - \overline{v}_{j\sigma}$$

$$(j = 1, \ldots, N_\sigma - 1), \tag{15}$$

where N_σ is the number of the orbitals with spin σ, and

$$M_{ji,\sigma} = \int d\vec{r}\frac{\rho_{j\sigma}(\vec{r})\rho_{i\sigma}(\vec{r})}{\rho(\vec{r})}, \tag{16}$$

$$\overline{V}_{j\sigma} = \langle\psi_{i\sigma}|\sum_{j=1}^{N_\sigma}\frac{\rho_{j\sigma}(\vec{r})v_{j\sigma}(\vec{r})}{\rho_\sigma(\vec{r})}|\psi_{i\sigma}\rangle. \tag{17}$$

As will be explained below, we will employ a grid representation in the three-dimensional coordinates to solve the Kohn-Sham equation. In this representation, it is practically impossible to describe core electrons, since the description of core electrons requires extremely fine grid spacing. We therefore describe only valence electrons, treating effects of the core electrons through the norm-conserving pseudopotentials. We thus ignore the ionization of core electrons and the influence of the core electrons through polarization, which are expected to be small. In the practical calculations, we employ the pseudopotentials constructed with a procedure of Troullier and Martins [26] and with a separable approximation [27],

$$v_{\mathrm{ps}}(\vec{r},\vec{r}') = v_{\mathrm{loc}}(r)\delta(\vec{r}-\vec{r}') + \sum_{lm}\frac{\Delta v_l^{\mathrm{p}}(r)\psi_{lm}^{\mathrm{p}}(\vec{r})\psi_{lm}^{\mathrm{p}*}(\vec{r}')\Delta v_l^{\mathrm{p}}(r')}{\int d\vec{r}|\psi_{lm}^{\mathrm{p}}(\vec{r})|^2\Delta v_l^{\mathrm{p}}(r)}. \tag{18}$$

The pseudopotential is constructed for each partial wave specified by the angular momentum l, which we denote as $v_l^{\mathrm{p}}(r)$. We include up to $l=2$. The pseudopotential with a certain angular momentum l_0 is adopted for the local one, $v_{\mathrm{loc}}(r)=v_{l_0}^{\mathrm{p}}(r)$. $\psi_{lm}^{\mathrm{p}}(\vec{r})$ is the atomic wave function for the partial wave lm calculated with the pseudopotential. Δv_l^{p} is defined by $\Delta v_l^{\mathrm{p}}(r)=v_l^{\mathrm{p}}(r)-v_{\mathrm{loc}}(r)$.

C. Boundary condition

To calculate the Gamow states, we need to solve the static Schrödinger equation, Eq. (4), with the outgoing boundary condition. For systems without spherical symmetry, the treatment of the outgoing boundary condition is not simple. Instead of imposing the outgoing boundary condition explicitly, we will employ the absorbing boundary condition (ABC) in which an imaginary (absorbing) potential is placed in the spatial region outside the molecule. Denote the radial distance from the center of the molecule as r. The absorbing potential is placed in the spatial region outside a certain radius R with a thickness $R<r<R+\Delta R$. Outside the region of the absorbing potential $r>R+\Delta R$, the wave functions are set to vanish. If the absorbing potential works ideally, there exist only the outgoing waves just inside the absorbing potential $r=R$.

In practice, we employ the following spherical absorbing potential with a linear radial dependence.

$$-iW(r) = \begin{cases} 0 & (0<r<R), \\ -iW_0\dfrac{r-R}{\Delta R} & (R<r<R+\Delta R), \end{cases} \tag{19}$$

where R is set beyond the barrier region. The height $W_0(>0)$ and the thickness ΔR are determined from the conditions that the electrons coming into the region $r>R$ should be absorbed as completely as possible. For the electrons with kinetic energy E, the parameters should satisfy the following condition [18]:

$$20\frac{E^{1/2}}{\Delta r\sqrt{8m}} < W_0 < \frac{1}{10}E^{(3/2)}\sqrt{8m}\Delta r, \tag{20}$$

where m is the electron mass.

Employing the absorbing potential, the Gamow state is obtained by solving the following Kohn-Sham equation:

$$\{h[n(\vec{r})] + V_{\text{ext}}(\vec{r}) - iW(\vec{r})\}\phi_i(\vec{r}) = (\epsilon_i^{\text{R}} + i\Gamma_i)\phi_i(\vec{r}), \tag{21}$$

with the vanishing boundary condition $\phi_i(\vec{r})=0$ for $|\vec{r}|>R+\Delta R$.

One may derive an expression for the ionization rate which includes the absorbing potential $W(\vec{r})$. To show it, we start with Eq. (10). We take a sphere of radius R for V and apply the Gauss theorem. Then we obtain the following expression for Γ_i:

$$\Gamma_i = -\frac{\int_{r>R} d\vec{r}|\phi_i(\vec{r})|^2 W(\vec{r})}{\int_{r<R} d\vec{r}|\phi_i(\vec{r})|^2}. \tag{22}$$

The total ionization rate w is given by summing up the rates of all occupied orbitals, $w=\Sigma_i w_i$. We may assume that the denominator of Eq. (22) is equal to a normalization constant, unity, so long as the ionization rate is not very large. Then the ionization rate is expressed as the following integral form including the absorbing potential $W(\vec{r})$ and the electron density $n(\vec{r})$,

$$w = -\frac{2}{\hbar}\sum_i \Gamma_i = \frac{2}{\hbar}\int_{r>R} d\vec{r}n(\vec{r})W(\vec{r}). \tag{23}$$

The ionization rate calculated in this way should coincide with the rate calculated from the imaginary part of the eigenvalue. In the practical calculation, this relation can be used as a useful check for the numerical calculation.

D. Numerical details

To express the orbital wave functions, we employ the real-space grid method. This is a convenient representation in the Kohn-Sham theory, since the potential is almost local in the coordinate representation. To impose the ABC, one must treat large spatial region far outside the molecule. The number of grid points becomes substantially large. To save the computational effort, we reduce the number of grid points employing the following adaptive grid.

The adaptive grid is generated as follows. We introduce the following coordinate transformation from (x,y,z) to (u,v,w) for each Cartesian, coordinate,

$$x = \frac{ku}{1+(k-1)\left(\dfrac{u}{a\,\sinh\dfrac{u}{a}}\right)^n}, \tag{24}$$

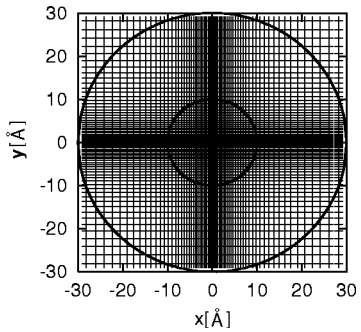

FIG. 1. The adaptive mesh that we use to solve the Kohn-Sham equation. The grid points inside the large circle are employed in the calculation. The orbital wave functions lie inside the small sphere when the external field is not applied. The absorbing potential is placed in the spatial region between two circles.

$$y = \frac{kv}{1+(k-1)\left(\dfrac{v}{a\,\sinh\dfrac{v}{a}}\right)^n}, \tag{25}$$

$$z = \frac{kw}{1+(k-1)\left(\dfrac{w}{a\,\sinh\dfrac{w}{a}}\right)^n}, \tag{26}$$

where a, k, and n determine the property of the transformation. By this transformation, there holds $x\sim u$ for small x ($x\ll a$), and $x\sim ku$ for large x ($x\gg a$). We then discretize uniformly the variable u,v,w. This produces a uniform grid for small x and a courser grid for large x. The grid points employed in the calculation are shown in Fig. 1. The transformation parameters to be used in the calculations are summarized in Table I. We have examined carefully that the results are not sensitive to the choice of the parameters.

As we mentioned in the last part of Sec. II A, the calculations of the ionization rates proceed in the following two steps. We first solve the static Kohn-Sham equation under the static dipole field described by $V_{\text{ext}}(\vec{r})=eFz$. At this stage, we suppress the emission of electrons to the continuum by placing a spherical wall potential outside the molecule. Namely, we solve the following Kohn-Sham equation:

TABLE I. The spatial parameters employed in the calculations of rare-gas atoms and diatomic molecules. R_{ps} is a radius of pseudopotential. R and ΔR are the radii related to the absorbing potential. h is a width of discretization of the variables u,v,w. a, k, and n are parameters which specify the adaptive coordinate transformation.

	R_{ps} (Å)	R (Å)	ΔR (Å)	h	a	k	n
Rare-gas atoms	1.4	10.0	20.0	0.2	5.0	10.0	2
Diatomic molecules	0.8	10.0	20.0	0.2	5.0	10.0	2

$$\{h[n(\vec{r})] + V_{\rm ext}(\vec{r}) + V_{\rm wall}(\vec{r})\}\phi_i(\vec{r}) = \epsilon_i\phi_i(\vec{r}), \qquad (27)$$

where $V_{\rm wall}(\vec{r})$ is set as

$$V_{\rm wall}(\vec{r}) = \begin{cases} 0 \text{ eV} & (r < R_{\rm wall}) \\ V_0 \text{ eV} & (r > R_{\rm wall}). \end{cases} \qquad (28)$$

The radial distance of the wall $R_{\rm wall}$ is so chosen that the final results of the ionization rate do not depend on it. In practice, we employ $R_{\rm wall}=6$ Å and $V_0=1000$ eV for all calculations. In solving the Kohn-Sham equation, Eq. (27), the conjugate gradient method is employed.

Once the self-consistent potential is obtained in the calculation with the wall potential, this potential is kept fixed in the calculation of the Gamow state. We remove the wall potential and add the absorbing potential $-iW(\vec{r})$ in Eq. (27).

The potential of the dipole external field eFz becomes quite large at the spatial region far apart from the origin of the molecule. The emitted electrons are accelerated strongly by this potential. This acceleration induces difficulty for the absorbing boundary condition: the fast electrons may not be absorbed efficiently by the absorbing potential. To remove the difficulty, we modify the external potential $V_{\rm ext}(\vec{r})$ from a dipole form eFz to a quadratic form outside the barrier region,

$$V_{\rm ext}(\vec{r}) = \begin{cases} eFz & (z < R_c) \\ eF\left[R_c + \dfrac{\Delta R_c}{2} - \dfrac{1}{2\Delta R_c}(z - R_c - \Delta R_c)^2\right] & (R_c < z < R_c + \Delta R_c) \\ eF\left(R_c + \dfrac{\Delta R_c}{2}\right) & (z > R_c + \Delta R_c). \end{cases} \qquad (29)$$

R_c is taken to be outside the barrier top and to be inside the radius of the absorbing potential R. The potential value at R_c, eFR_c should be larger than the ionization potential of the molecule. In practice, we take $R_c \simeq 8-10$ Å.

The final problem is to calculate the Gamow state by solving Eq. (21), in which the density $n(\vec{r})$ is kept fixed to that obtained with the wall potential. This is not a Hermitian problem. We have found that this equation can be solved efficiently with the shifted inverse iteration method [28]. For each orbital specified by i, the algorithm is given as follows:

Start. Prepare an initial guess for the wave function $\psi_i^{(0)}(\vec{r})$ and the shift ξ.

Iterate. For $k=1,2,\cdots$ until convergence, compute

$$\psi_i^{(k)}(\vec{r}) = \frac{1}{\alpha_k}\{h[n(\vec{r})] + V_{\rm ext} - iW(\vec{r}) - \xi\}^{-1}\psi_i^{(k-1)}(\vec{r}), \quad (30)$$

where α_k is a normalization factor.

As an initial guess for the wave function $\psi_i^{(0)}(\vec{r})$, we utilize the static Kohn-Sham solution with the wall potential. The shift ξ is also taken as the real eigenvalue of the Kohn-Sham solution with the wall potential. To calculate $\psi_i^{(k)}$ defined by Eq. (30), we solve the following Schrödinger-like equation with a source term:

$$\{h[n(\vec{r})] + V_{\rm ext} - iW(\vec{r}) - \xi\}\psi_i^{(k)}(\vec{r}) = \psi_i^{(k-1)}(\vec{r}). \qquad (31)$$

In the real-space grid representation, this equation can be regarded as a linear algebraic equation with a sparse matrix with complex elements. To solve this equation, we have found the conjugate residual method works efficiently.

In some cases, there are almost degenerate eigenvalues for which the above simple shifted inverse iteration method fails to provide all independent solutions. In that case, we employ the deflation technique [28] where the vector space which was obtained as eigenfunctions in the previous steps is removed in the iteration procedure.

III. RESULTS AND DISCUSSIONS

A. Rare-gas atoms

We first report calculated results of the rare-gas atoms Ar and Xe. We show in Fig. 2 the self-consistent potential for Xe atom obtained by solving Eq. (27). In the left panel, the potentials are shown along the axis parallel to the external field for three cases of different external field. The origin is set at the center of the atom. The energy of the highest occupied orbital is denoted by the horizontal lines. The barrier energy gets lower as the external field increases, while the change of the orbital energy by the Stark effect is small and is not seen. In the right panel, the self-consistent potential is plotted in the plane which includes the center of the atom and is parallel to the external field. The strength of the field is set at 5×10^{13} W/cm^2 (1.94 eV/Å). The bold line indicates the orbital energy of the highest occupied orbital, −12.3 eV.

To calculate the Gamow states, we solve Eq. (21) which includes the absorbing potential. In Fig. 3, we show the behavior of the ionization rate of Xe atom when we change the parameter W_0 of the absorbing potential. To demonstrate W_0 dependence clearly, we choose a small radius for the absorbing potential, $\Delta R=8$ Å in this calculation. For all other calculations, we employ much larger radius, $\Delta R=20$ Å as we wrote in Table I. The laser intensity is fixed at 5×10^{13} W/cm^2. At this intensity, the kinetic energy of emitted electron is about 7 eV in the spatial region $r\sim R+\Delta R$. Under these conditions, the appropriate value of W_0 from Eq.

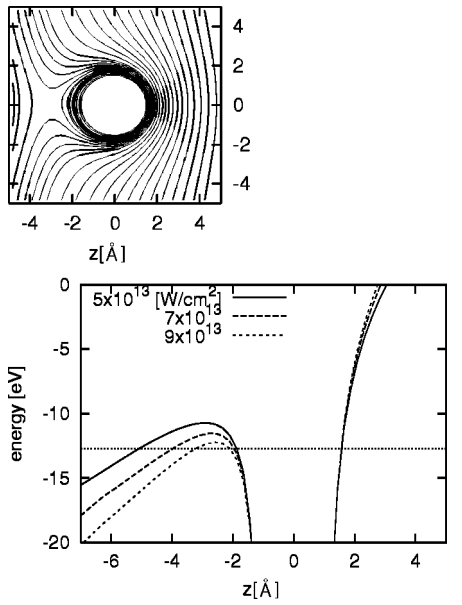

FIG. 2. Self-consistent potential of Xe atom in the strong electric field. The left-hand panel shows the potential along the direction of the electric field for three cases of external electric field. The right-hand panel shows contour lines of the potential in a plane parallel to the direction of the electric field at the strength of 5×10^{13} W/cm^2.

(20) is restricted as 7 eV$<W_0<$16 eV. Figure 3 shows that the ionization rate is almost constant in the wide region of the parameter W_0. Smaller W_0 gives too small an ionization rate, because of the insufficient absorption and reflection at $r=R+\Delta R$. Larger W_0 also results in too small an ionization rate, because of the reflection at $r=R$ caused by the absorbing potential. Employing wide spatial region of absorbing potential, $\Delta R=20$ Å, there are wide regions of parameter W_0 where the ionization rate is not sensitive to the choice of the parameter. For all the results shown below, we examined carefully that the calculated ionization rates are not sensitive to the change of W_0.

In Table II, we show the orbital energies of the Gamow states of Xe atom for p_x, p_y, and p_z orbitals. The external field is set parallel to the z axis. Since we employ self-interaction correction, the absolute values of the orbital energies are very close to the ionization potential. The calculated p orbital energy in the absence of the laser field is 12.07 eV. The electric field reduces the symmetry of the system from spherical to axial. The complex eigenvalues of the p_x and p_y orbitals are the same reflecting the axial symmetry. As seen in the table, the ionization rate of the p_z orbital is larger by 1–2 order of magnitude than those of p_x and p_y. The eigenvalue of the s orbital is not shown, since the imaginary part of the eigenvalue of the s orbital is very small.

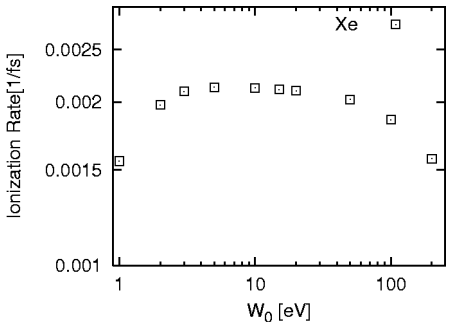

FIG. 3. W_0 dependence of ionization rate of Xe atom. Laser intensity is 5×10^{13} W/cm^2.

Summing up the ionization rates of all orbitals, we obtain the total ionization rate. In Fig. 4, we show the calculated ionization rate of the Xe and Ar atoms by open squares. The measurements are available with the linear polarized, ultrashort (30 fs) laser at 800 nm [29]. In the measurements, relative ionization rates at various laser intensities are available. We plot the measured rates in the figure, normalizing the measurements to coincide with the calculation at the laser intensity of 9×10^{13} W/cm^2 for Xe atom, and at the laser intensity of 1.3×10^{14} W/cm^2 for Ar atom. We also plot the rate in the ADK theory by the dotted curve. Since we show the rate for a static field, we compare the rate expression in the ADK theory for a static field. The rate expression for the static field w_{static} is related to the rate expression for the periodic one, $w_{periodic}\times w_{periodic}=\sqrt{3F/\pi\kappa^3}w_{static}$ with $\kappa=\sqrt{2I_P}$.

As seen in the figure, the measured dependence on the laser intensity is described fairly well by the calculation. The calculated rate decreases much faster than the measurements when the laser intensity is weak ($<3\times10^{13}$ W/cm^2 for Xe and $<6\times10^{14}$ W/cm^2 for Ar). This trend may be attributed to the effect of the multiphoton process. Comparing our calculation with the ADK formula, the absolute values of the ionization rate are slightly higher (about a factor of 2) for all the region of the laser intensity. Thus the laser intensity dependence is very similar between our calculation and the

TABLE II. Orbital energy of each Gamow state of Xe atom is shown under the static electric field parallel to the z axis. The measured ionization potential is denoted as well. Numbers in brackets denote powers of 10.

Laser intensity (W/cm^2)	$2p_x$ (eV)	$2p_y$ (eV)	$2p_z$ (eV)	IP (eV)
4×10^{13}	−12.27-i1.07[−5]	−12.27-i1.07[−5]	−12.30-i1.99[−4]	12.13
5×10^{13}	−12.33-i2.22[−5]	−12.33-i2.22[−5]	−12.38-i7.04[−4]	
6×10^{13}	−12.39-i5.13[−5]	−12.39-i5.13[−5]	−12.47-i1.85[−3]	
7×10^{13}	−12.47-i1.32[−4]	−12.47-i1.32[−4]	−12.56-i3.68[−3]	
8×10^{13}	−12.56-i2.55[−4]	−12.56-i2.55[−4]	−12.69-i8.65[−3]	
9×10^{13}	−12.67-i5.93[−4]	−12.67-i5.93[−4]	−12.79-i1.11[−2]	

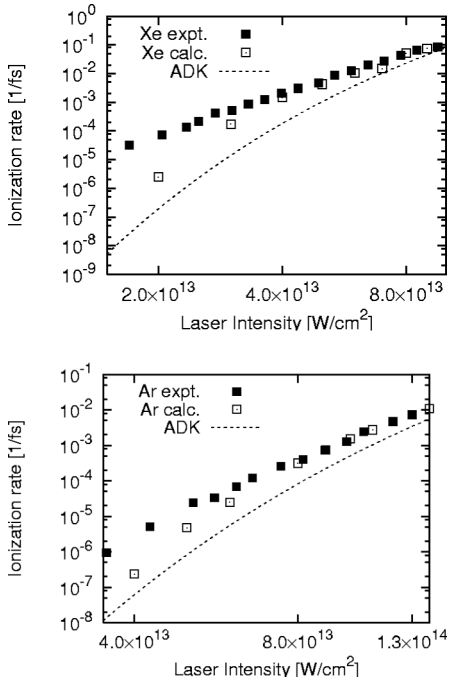

FIG. 4. Ionization rates of neutral Xe and Ar atoms are shown as a function of the laser intensity. Open squares denote our calculation. Filled squares are the measured results [29] whose absolute values are normalized to coincide with the calculation at a certain laser intensity, 9×10^{13} W/cm^2 for Xe atom and 1×10^{14} W/cm^2 for Ar atom.

ADK results. This indicates the usefulness of the ADK theory in describing the relative ionization rates of atoms with many electrons for wide laser intensities.

The present calculation incorporates many-electron effects through the realistic self-consistent potential generated by solving Eq. (27). Beyond single electron approximation, the screening effect due to the static polarization of atom is taken into account. We examined the effect of the screening on the ionization. In Fig. 5, we show the ionization rate when one ignores the static polarization. This is achieved by calculating the Kohn-Sham Hamiltonian without the external potential V_{ext} in Eq. (27) and then employing this Hamiltonian in Eq. (21). Without the static polarization, the ionization rates of Ar atom are slightly higher, about a factor of 2, than those with the polarization. The dependence on the laser intensity is not much affected by the polarization.

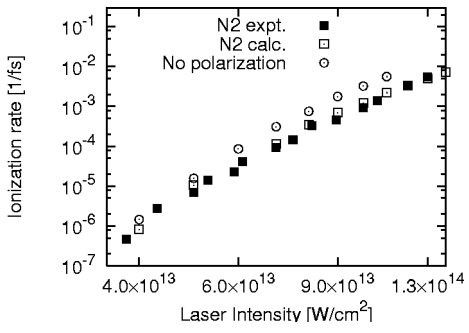

FIG. 5. The ionization rates of Ar atom with and without incorporating the static polarization are compared. The open squares show ionization rates with the polarization, while the open circles without the polarization. Filled squares are the measured results [29] which is normalized as denoted in the caption of Fig. 4.

B. Molecules: N_2, O_2, and F_2

We next show results of tunnel ionization rates for diatomic molecules, N_2, O_2, and F_2. We first show the Kohn-Sham eigenvalues and molecular-orbital properties of the diatomic molecules without external field in Table III. The measured ionization potentials of N_2, O_2, and F_2 are 15.58 eV, 12.06 eV, and 15.70 eV, respectively. As mentioned previously, the measured ionization potentials and the calculated highest occupied molecular orbital (HOMO) energies are close to each other, since we employ the self-interaction correction. The agreement is, however, less accurate for these diatomic molecules in comparison with the agreement in rare-gas atoms. The HOMO orbital energies of O_2 and F_2 are about 1 eV smaller than the ionization potential.

We note that the properties of HOMO orbitals are different among molecules: The HOMO of the N_2 is the σ orbital, having zero angular momentum around the symmetry axis. On the other hand, the HOMO orbitals of O_2, and F_2 are π^*, having one-unit angular momentum around the symmetry axis and having also the nodal plane perpendicular to the molecular axis. The O_2 molecule has a spin-triplet ground state. We employ local spin-density approximation (LSDA) for this molecule, these spin properties induce difference between the HOMO orbitals of O_2 and F_2. Namely, four electrons occupy degenerate π^* orbitals in F_2, while two electrons occupy degenerate π^* orbitals in O_2.

We show the calculated ionization rates of these molecules, and investigate the relationship between the ionization rates and the molecular-orbital properties. The difference of the orbital property manifests clearly in the angle dependence of the ionization rate. Figure 6 shows the angle dependence of the ionization rates of N_2 and O_2 molecules. The angle is measured between the molecular axis and the external field. If we ignore the properties of the molecular orbital, one may expect that the ionization rate shows maximum when the external field is parallel to the molecular axis. The calculated ionization rate of N_2 molecule, whose HOMO orbital has the σ character, indeed shows maximum when the external field is parallel to the molecular axis.

However, the angle dependence of the ionization rate of O_2 molecule is quite different. The ionization is strongly suppressed when the external field is either parallel to or perpendicular to the molecular axis. A similar angle dependence is also found for F_2. These suppressions of the rate for a certain directions can be understood from the properties of the HOMO, the π^* orbital, in O_2 and F_2. To obtain more intuitive understanding, we show in Fig. 7 the electron-density distribution of the HOMO orbital of O_2 molecule under the external field changing the relative angle between the external field and the molecular axis. The nodal structures in the plane perpendicular to the molecular axis, as well as in the symmetry axis along the molecular axis, are clearly seen.

TABLE III. Molecular orbitals of diatomic molecules, N_2, O_2, and F_2 are shown. The N_2 and F_2 are calculation in which two electron occupy the same spatial orbital, while O_2 is calculated in the local spin-density approximation with self-interaction correction. The calculated orbital energies and orbital characters are shown.

N_2		O_2			F_2	
Orbital	Up and down	Orbital	Up	Down	Orbital	Up and down
σ	−14.90	π^*	−11.29		π^*	−14.40
π	−16.88	π^*	−11.29		π^*	−14.40
π	−18.82	π	−18.54	−17.29	π	−18.12
σ	−17.78	π	−18.54	−17.29	π	−18.12
σ	−33.47	σ	−18.45	−18.55	σ	−20.50
		σ^*	−24.53	−23.20	σ^*	−31.81
		σ	−38.09	−38.16	σ	−38.89

The electron density is maximally extended spatially at the angle $\pi/4$, where the ionization rate shows maximum. Thus the ionization is strongly influenced by the molecular-orbital properties of the HOMO. This point has also been stressed in the molecular ADK treatment by Tong *et al.* [24].

Recently, the angle dependence of the ionization rate has been measured for N_2 molecule [30]. In the left panel of Fig. 6, we compare calculated angle dependence of the ionization rate with a function which is one of those functions that can explain measurement. Two curves are normalized to coincide at the forward angle. Qualitative behavior is similar between our calculation and the function, showing maximum when the molecular axis is parallel to the external field and minimum when the molecular axis is perpendicular to the external field. However, the calculated angular dependence is much weaker than that which explains measurement. We note that the laser intensity in our calculation, 1×10^{14} W/cm^2, is smaller than the intensity in the measurement (2×10^{14} W/cm^2). The latter intensity corresponds to the boundary between the tunnel and the above barrier mechanisms. The discrepancy between our calculation and the measurement may originate from this change of the ionization mechanism. Our method cannot be applicable to the case of latter intensity where the ionization rate is large.

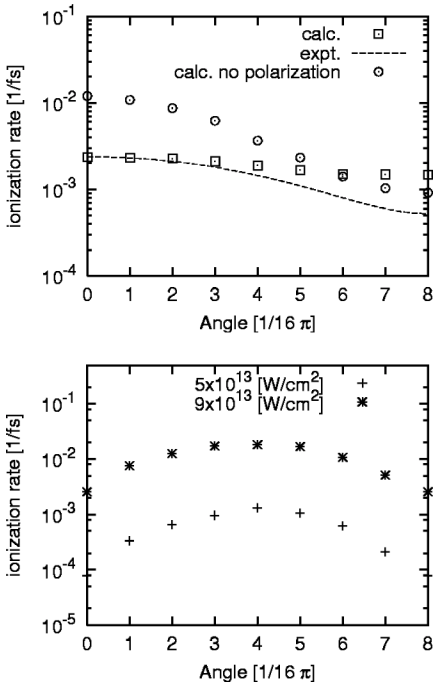

FIG. 6. Angle dependence of ionization rate for N_2 (left panel) and O_2 (right panel) molecules. The angle is measured between the external field and the molecular axis. In the N_2 calculation, the calculations with and without the polarization effect are shown by open square and circles, respectively. The dashed curve indicates a distribution which explains measurement [30]. For O_2 case, angle dependences for the cases of two different laser intensities are shown.

Integrating the angle dependent ionization rate over molecular orientation, we obtain the ionization rate of the molecule. Since it costs much to calculate the angle dependence

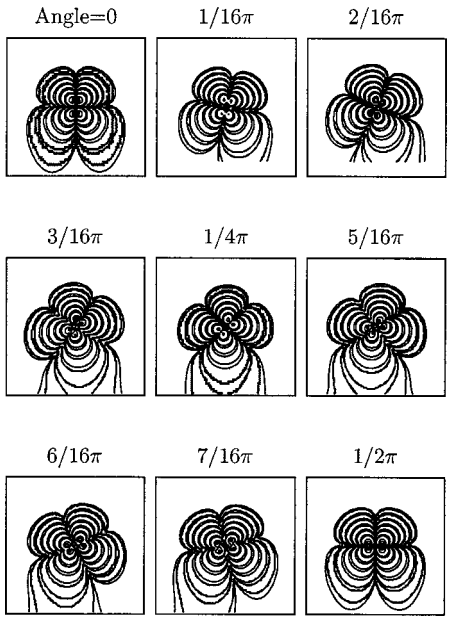

FIG. 7. Density of electron in the highest occupied orbital of O_2 molecule. The direction of the laser field is always taken to be vertical direction, while the molecular axis is rotated.

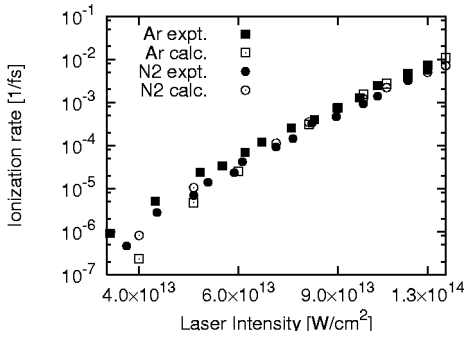

FIG. 8. The ionization rates of N_2 and Ar are shown as a function of the laser intensity. The measured rates are scaled in such a way that the measured rate of Ar at 1.3×10^{14} W/cm^2 coincides with the calculation.

for each laser intensity, we calculate the ionization rates at the angle with maximum ionization rate (0° for N_2 and 45° for O_2 and F_2), and rescale them to obtain the angle-integrated rates assuming that the angle dependence does not depend much on the laser intensity.

In Fig. 8, we show the calculated ionization rate of N_2 as a function of the laser intensity. The ionization rate of Ar atom whose ionization potential is close to that of N_2 is also plotted. In the measurements, the absolute value of the rate is not available. As before, we scaled the measured rate of Ar atom to coincide with the calculation at laser intensity of 1.3×10^{14} W/cm^2. We note that the relative intensity between Ar and N_2 has been measured and is reliable. The calculation nicely reproduces the relative ionization rates between Ar and N_2 as well as the laser intensity dependence. The dependence on the laser intensity is very similar between N_2 and Ar.

For molecules, screening effect by the polarization of other electrons is expected to be more significant. To see the effect of the static polarization on the ionization rate, we made a calculation suppressing the polarization. As we did for Ar atom case, we construct Kohn-Sham Hamiltonian without external field, and employ this Hamiltonian in the Gamow state calculation. In Fig. 9, we show the ionization rates with and without incorporating the effect of the polarization. If one omits the polarization effect, the ionization rate becomes about two to five times larger. Thus the effect of the polarization is indeed more significant for molecule case. The polarization effect does not affect much on the

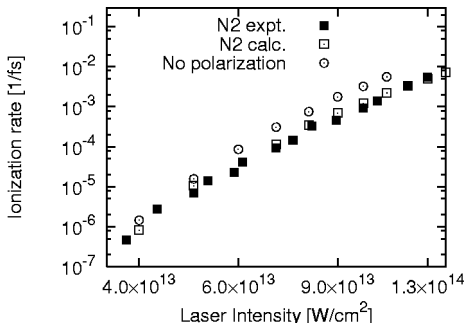

FIG. 9. The ionization rates of N_2 molecule with and without screening are compared.

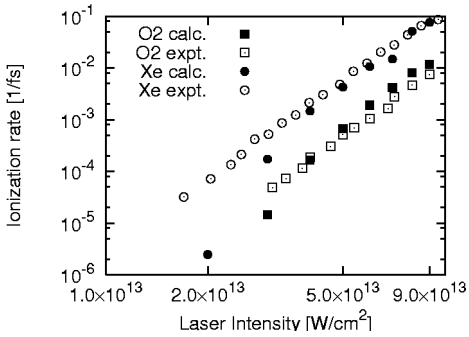

FIG. 10. Ionization rates of Xe atom and O_2 molecule as a function of the laser intensity. Open circles and open squares are our calculations for Xe and O_2, respectively. Filled circles and filled squares are measured rates at wavelength 800 nm and laser pulse length of 30 fm. The measured rates are scaled in such a way that the measured rate of Xe at 9×10^{13} W/cm^2 coincides with the calculation.

dependence on the laser intensity. In the left panel of Fig. 6, we show calculated angle dependence when the polarization effect is excluded. The ionization is strongly suppressed when the external field is parallel to the molecular axis. This is consistent with the fact that the static polarizability is the largest when the external field is parallel to the molecular axis.

We next turn to the ionization of O_2 molecule. In Fig. 10, we compare the ionization rate of Xe atom and O_2 molecule. The measured ionization rate is also plotted. As before, we scaled the measured rate of Xe atom so that the calculated rate coincides with the measurement at the laser intensity of 9×10^{13} W/cm^2. The relative ionization rate of Xe atom and O_2 molecule shows marked difference, in spite of the similar ionization potential between two systems. Our calculation succeeds to reproduce this feature. This strong suppression of the ionization rate in O_2 molecule is clearly related to the angle dependence of the ionization rate discussed above. Because the π^* orbital vanishes along the molecular axis, the ionization to the direction parallel to the molecular axis is strongly suppressed. In other words, the π orbital feels the centrifugal barrier along the molecular axis. This centrifugal barrier hinders the emission of the electrons along the molecular axis.

The calculated suppression of the ionization rate for O_2 molecule is not enough to explain fully the measured suppression. One possible origin of this discrepancy is a limited accuracy of the orbital energy in our approach. The ionization potential of O_2 molecule is 12.06 eV. However, in our calculation with the self-interaction correction, the orbital energy of the HOMO is −11.29 eV. If we could manage to shift the HOMO energy so as to reproduce the measured ionization potential, we may expect that the calculated ionization rate would be suppressed further.

We next consider briefly the ionization of F_2 molecule. The ionization potential of F_2 is close to those of Ar and N_2. Figure 11 shows a comparison of calculated ionization rate of Ar, N_2, and F_2. The ionization rate of F_2 is smaller than those of Ar and N_2. Since the HOMO of F_2 is a π^* orbital, the same mechanism as that of O_2 is expected. The suppres-

sion is, however, not very strong compared with the suppression for O_2 molecule. One of the reasons of this difference between O_2 and F_2 is the different occupation number of the HOMO orbital. The HOMO of F_2 is occupied by four electrons, while the HOMO of O_2 is occupied by two, reflecting the triplet structure of the O_2.

In the measurements, a strong suppression of the ionization rate is not reported for F_2. Our results may look consistent with this observation. However, in our calculation, the HOMO orbital energy of F_2 is 14.40 eV while the measured ionization potential is 15.70 eV. Therefore, our calculation should have overestimated the ionization rate. To get conclusive results, we feel that further analysis are required employing a better functional which describes orbital energies consistent with the measured ionization potential.

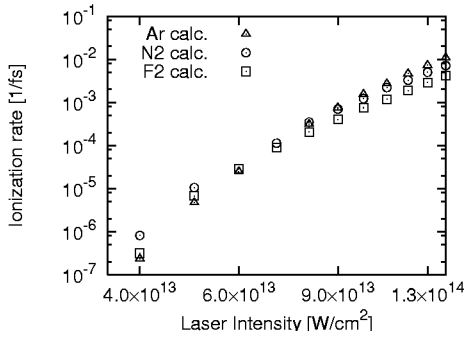

FIG. 11. Calculated ionization rates of F_2 are compared with those of Ar and N_2.

IV. SUMMARY

We present first-principles calculations of the ionization rates of some atoms and molecules under static dipole field. A new computational method is developed based on the Kohn-Sham formalism. The Gamow states are calculated in real-space discretizing the three-dimensional coordinates and introducing the absorbing boundary condition. The ionization rates are then obtained from the imaginary part of the Gamow state eigenvalues.

The ionization rates of rare-gas atoms Ar and Xe and homonuclear diatomic molecules, N_2, O_2, and F_2 are calculated. Our calculations nicely reproduces overall features of the measured ionization rates including the dependence on the laser intensity. They also show good correspondence with the Ammosov-Delone-Krainov model for rare-gas atoms.

The ionization rate of the diatomic molecules are strongly influenced by the properties of the HOMO. The HOMO of the N_2 is the σ orbital, while the HOMO's of O_2 and F_2 are the π^* orbital. The ionization rates show characteristic angle dependence between the molecular axis and the laser direction. The ionization rate of N_2 does not depend much on the orientation, while the rates of O_2 and F_2 are strongly suppressed along the molecular axis and to the plane perpendicular to the molecular axis. The property of the HOMO orbital also has a significant effect on the absolute value of the ionization rate. The measured suppression of the ionization rate of O_2 molecule in comparison with that of Xe is nicely reproduced by our calculation.

The present analysis is achieved in the static limit, ignoring the oscillatory effect of the external field. With the real-space grid representation, calculations of the three-dimensional electron dynamics are feasible. The extension toward this direction is now under progress.

ACKNOWLEDGMENTS

This work is supported by the Grant-in-Aid for Scientific Research (Grant No. 14540369), and also by NAREGI Nanoscience Project, Ministry of Education, Culture, Sports, Science and Technology, Japan. Numerical calculations are achieved on the supercomputers at the Institute for Solid State Physics, University of Tokyo, and at the Research Center for Nuclear Study (RCNP), Osaka University.

[1] L. V. Keldysh, Sov. Phys. JETP **20**, 1307 (1965).
[2] A. M. Ammosov, N. B. Delone, and V. P. Krainov, Sov. Phys. JETP **64**, 1191 (1986).
[3] F. H. M. Faisal, J. Phys. B **6**, L89 (1973).
[4] H. R. Reiss, Phys. Rev. A **22**, 1786 (1980).
[5] J. L. Krause, K. J. Schafer, and K. C. Kulander, Phys. Rev. A **45**, 4998 (1992).
[6] S. Chelkowski, T. Zuo, and A. D. Bandrauk, Phys. Rev. A **46**, R5342 (1992).
[7] T. Zuo and and A. D. Bandrauk, Phys. Rev. A **52**, R2511 (1995).
[8] I. Kawata, H. Kono, and Y. Fujimura, Chem. Phys. Lett. **289**, 546 (1998).
[9] I. Kawata, H. Kono, and Y. Fujimura, J. Chem. Phys. **110**, 11 152 (1999).
[10] C. A. Ullrich, P.-G. Reinhard, and E. Suraud, J. Phys. B **30**, 5043 (1997).
[11] C. A. Ullrich, P.-G. Reinhard, and E. Suraud, J. Phys. B **31**, 1871 (1998).
[12] F. Calvayrac, P.-G. Reinhard, E. Suraud, and C. A. Ullrich, Phys. Rep. **337**, 493 (2000).
[13] X. Chu and S.-I. Chu, Phys. Rev. A **63**, 023411 (2001).
[14] X.-M. Tong and S.-I. Chu, Phys. Rev. A **64**, 013417 (2001).
[15] K. Yabana and G. F. Bertsch, Phys. Rev. B **54**, 4484 (1996).
[16] K. Yabana and G. F. Bertsch, Int. J. Quantum Chem. **75**, 55 (1999).
[17] G. F. Bertsch, J.-I. Iwata, A. Rubio, and K. Yabana, Phys. Rev. B **62**, 7998 (2000).
[18] T. Nakatsukasa and K. Yabana, Phys. Rev. A **114**, 2550 (2001).
[19] J.-I. Iwata, K. Yabana, and G. F. Bertsch, J. Comp. Meth. Sci. Eng. (to be published).
[20] R. Nagano, K. Yabana, T. Tazawa, and Y. Abe, Phys. Rev. A **62**, 062721 (2000).
[21] A. Talebpour, C. Y. Chien, and S. L. Chin, J. Phys. B **29**, L677 (1996).

[22] M. J. DeWitt, E. Wells, and R. P. Jones, Phys. Rev. Lett. **87**, 153001 (2001).
[23] J. Muth-Böhm, A. Becker, and F. H. M. Faisal, Phys. Rev. Lett. **85**, 2280 (2000).
[24] X. M. Tong, Z. X. Zhao, and C. D. Lin, Phys. Rev. A **66**, 033402 (2002).
[25] J. B. Krieger, Y. Li, and G. J. Iafrate, Phys. Rev. A **45**, 101 (1992).
[26] N. Troullier and J. L. Martins, Phys. Rev. B **43**, 1993 (1991).
[27] L. Kleinman and D. Bylander, Phys. Rev. Lett. **48**, 1425 (1982).
[28] Y. Saad, *Numerical Methods for Large Eigenvalue Problems*, Sec. IV (Manchester University Press, Manchester, 1992).
[29] C. Guo, M. Li, P. Nibarger, and G. N. Gibson, Phys. Rev. A **58**, R4271 (1998).
[30] I. V. Litvinyuk, K. F. Lee, P. W. Dooley, D. M. Rayner, D. M. Villeneuve, and P. B. Corkum, Phys. Rev. Lett. **90**, 233003 (2003).